Fast, high-contrast imaging of animal development with scanned light sheet–based structured-illumination microscopy

Philipp J Keller[1,2], Annette D Schmidt[3], Anthony Santella[4], Khaled Khairy[1], Zhirong Bao[4], Joachim Wittbrodt[3,5] & Ernst H K Stelzer[1,6]

Recording light-microscopy images of large, nontransparent specimens, such as developing multicellular organisms, is complicated by decreased contrast resulting from light scattering. Early zebrafish development can be captured by standard light-sheet microscopy, but new imaging strategies are required to obtain high-quality data of late development or of less transparent organisms. We combined digital scanned laser light-sheet fluorescence microscopy with incoherent structured-illumination microscopy (DSLM-SI) and created structured-illumination patterns with continuously adjustable frequencies. Our method discriminates the specimen-related scattered background from signal fluorescence, thereby removing out-of-focus light and optimizing the contrast of in-focus structures. DSLM-SI provides rapid control of the illumination pattern, exceptional imaging quality and high imaging speeds. We performed long-term imaging of zebrafish development for 58 h and fast multiple-view imaging of early *Drosophila melanogaster* development. We reconstructed cell positions over time from the *Drosophila* DSLM-SI data and created a fly digital embryo.

Powerful new quantitative approaches to developmental biology have emerged that aim at understanding morphogenesis, developmental genetics and their relationship system-wide[1–9]. It is now possible to comprehensively follow cell behavior during the first day of zebrafish development[6] or to perform large-scale mapping of gene expression profiles in nematodes[9]. Such large-scale and high-throughput studies rely on advanced fluorescence microscopy and automated approaches to image processing and data analysis. The robustness of these approaches, however, depends substantially on the performance of the light microscope.

Recently, we developed digital scanned laser light sheet fluorescence microscopy (DSLM), in which a single plane in a specimen is quickly scanned with a thin laser beam while a camera-based detection arm records a fluorescence image at a right angle to the illumination axis. This approach provides a combination of crucial properties: imaging speed and signal-to-noise ratio are high, and the energy load on the specimen, and thus photobleaching and phototoxicity, are kept at a minimum[6,7]. Early zebrafish embryos can be recorded for up to 24 h and yield image data, from which cell movements can be reconstructed with high fidelity. However, similar analyses at later stages of embryogenesis or for less transparent specimens, such as *Drosophila melanogaster* embryos, are hampered by substantially increased light scattering. Image quality and contrast suffer when imaging highly complex multicellular specimens with many cell membranes that act as refractive interfaces or in embryos, in which somatic cells are engulfed by a lipid-rich yolk (for example, early *Drosophila* embryos).

To address this limitation, we previously introduced incoherent structured-illumination microscopy[10] to light sheet–based imaging[11] by placing a mechanical ruling in a conjugate image plane in the illumination arm of a selective plane illumination microscope[12] (a method named selective plane illumination microscopy with structured illumination; SPIM-SI) to illuminate the specimen with a fixed pattern of stripes rather than a homogeneous light sheet. Acquiring a shift series of images at different spatial phases of this pattern allowed us to discriminate the scattered background light against signal fluorescence using a simple processing algorithm. Unfortunately, the entire ruling had to be shifted to change the phase of the profile, and different rulings were required for different frequencies. SPIM-SI, therefore, suffered from low image quality, low imaging speed and the lack of flexibility regarding the shape and frequency of the illumination pattern[12].

Here we present a DSLM implementation of structured illumination (DSLM-SI) that addresses all three issues. In DSLM-SI, the intensity of the illuminating laser beam is electronically modulated in synchrony with the scanning process. This allowed us to create high-quality sinusoidal intensity profiles. Harmonic components, phase and frequency of the structured-illumination pattern are flexible and can be quickly adjusted to address spatiotemporal

[1]Cell Biology and Biophysics Unit, European Molecular Biology Laboratory, Heidelberg, Germany. [2]Janelia Farm Research Campus, Howard Hughes Medical Institute, Ashburn, Virginia, USA. [3]Institute of Zoology, Department for Developmental Physiology, University of Heidelberg, Heidelberg, Germany. [4]Developmental Biology Program, Sloan-Kettering Institute, New York, New York, USA. [5]Institute of Toxicology and Genetics, Karlsruhe Institute of Technology, Karlsruhe, Germany. [6]Frankfurt Institute for Molecular Life Sciences, Goethe University, Frankfurt am Main, Germany. Correspondence should be addressed to P.J.K. (kellerp@janelia.hhmi.org) or E.H.K.S. (stelzer@embl.de).

RECEIVED 27 JANUARY; ACCEPTED 26 MAY; PUBLISHED ONLINE 4 JULY 2010; DOI:10.1038/NMETH.1476

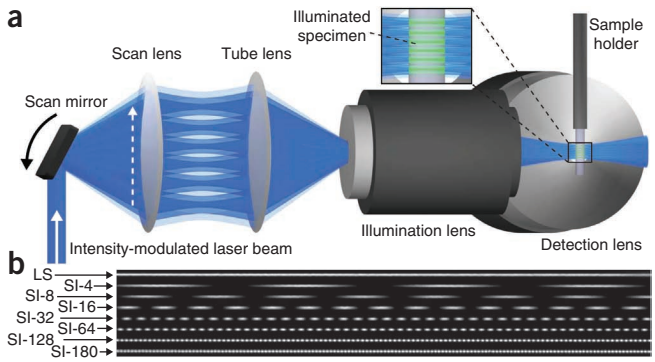

Figure 1 | Light sheet–based structured illumination with digitally adjustable frequency. (**a**) Side view of the central components of a digital scanned laser light-sheet fluorescence microscope. The illumination lens illuminates a thin volume by rapidly scanning a micrometer-sized laser beam through the specimen. Fluorescence is detected at a right angle to the illuminated plane by the detection lens. The intensity of the laser beam is modulated in synchrony with the scanning process. (**b**) Cross-sections of DSLM and DSLM-SI illumination profiles, recorded at 10× magnification. A uniform intensity distribution is used in the standard DSLM light-sheet illumination mode (LS). In the DSLM-SI mode, the spatial laser light intensity distribution is modulated in a sinusoidal fashion. The patterns shown here as reflections of a mirror oriented at 45° to the incident laser beam range from four sine periods (SI frequency $s = 4$; SI-4) to 180 sine periods (SI frequency $s = 180$; SI-180) across the field of view. The width of the image corresponds to a field size of 1.5 mm. Center-to-center distances of the maxima in the patterns range between 412.5 µm (SI-4) and 9.2 µm (SI-180).

changes of light-scattering properties in live specimens. DSLM-SI combines the strengths of DSLM with the contrast-enhancing properties of incoherent structured illumination, enabling fast physiological imaging of large multicellular specimens at high quality. We used DSLM-SI in several applications: high-speed imaging of early zebrafish development with multiple markers, long-term imaging of zebrafish development for up to 3 d and high-speed, multiple-view imaging of early *Drosophila* embryonic development. We demonstrate the potential of our technique by computationally reconstructing the *Drosophila* multiple-view time-lapse recording, generating a fly digital embryo.

RESULTS

High-quality planar structured-illumination patterns

The central idea in DSLM is to image a micrometer-thick volume by vertically scanning a thin laser beam that enters the specimen from the side (**Fig. 1a**). The fluorescence emitted in this volume is detected with a second lens arranged at a right angle to the illumination axis and imaged on a charge-coupled device (CCD) camera chip (**Supplementary Fig. 1**). Three-dimensional imaging can be performed either by scanning the light sheet through the specimen via a second scan mirror or by moving the specimen through the illuminated plane. To create structured-illumination patterns, we took advantage of the fact that the DSLM light sheet is created in a time-dependent manner: while the illuminating laser beam was scanned vertically through the specimen, we electronically modulated the intensity of the beam (**Supplementary Video 1**) with an acousto-optical tunable filter (AOTF). We changed the intensity of the laser beam with a response time of less than 10 µs by modulating the amplitude of the radio frequency input of the AOTF. Using a CCD camera, we measured the light intensity as a function of the amplitude of the radio frequency and then constructed a look-up table to reproduce a linear intensity scale. We applied the look-up table to create sinusoidal light intensity modulations with a specific phase and frequency, which we converted into the spatial frequency of a structured-illumination pattern by synchronizing the AOTF modulation with the linear movement of the laser scanner during specimen illumination (**Fig. 1**).

Changes in phase and frequency of the resulting structured-illumination pattern can be applied rapidly and precisely, owing to the electronic implementation of the modulation. We confirmed the high quality of the pattern by recording and analyzing the illumination profile directly with a CCD camera (**Supplementary Figs. 2** and **3**) as well as by scanning and reconstructing the surface of a small mirror in the DSLM-SI mode (**Supplementary Fig. 4a**). The comparison of the DSLM-SI reconstruction to the corresponding image in the standard DSLM light-sheet mode revealed practically artifact-free imaging in DSLM-SI (**Supplementary Fig. 4b–d**).

Contrast enhancement in DSLM-SI

Incoherent structured illumination provides the direct optical means for separating high-quality information (nonscattered signal photons) from low-quality background (scattered signal photons) in the recorded images. We analyzed the capabilities of DSLM-SI first by three-dimensional imaging of tissue phantoms for a wide range of scattering coefficients ($\mu_s = 1$–$15\ \mathrm{mm}^{-1}$; **Supplementary Fig. 5a** and **Supplementary Table 1**). To obtain a corrected image, we recorded each plane three times using three different phases of the structured-illumination pattern (0°, 120° and 240°). A new image I is calculated from each set of frames ($I_{0°}$, $I_{120°}$ and $I_{240°}$) using the formula[10]:

$$I = \sqrt{\frac{1}{2}\left(\left(I_{0°} - I_{120°}\right)^2 + \left(I_{120°} - I_{240°}\right)^2 + \left(I_{240°} - I_{0°}\right)^2\right)} \quad (1)$$

In this processing step, all nonmodulated parts were removed in the new image. The use of incoherent structured illumination[10] should not be confused with coherent structured illumination[13–16], which is based on the interference of multiple beams. Incoherent structured illumination takes advantage of the fact that the optical properties of a specimen affect the modulation pattern. Volume elements that scatter the light 'lose' the modulation of the illumination pattern. These regions are therefore similarly represented in the three phases, and subtracting the images according to equation 1 will effectively reduce the background to zero. A comparison of the DSLM-SI recordings with the corresponding standard DSLM light-sheet recordings demonstrated an average 533% ± 47% (s.d., $n = 7$ phantoms) increase in image contrast in DSLM-SI for the entire range of scattering coefficients investigated using tissue phantoms (**Supplementary Figs. 6** and **7**; we characterized each phantom in 2,500 measurement conditions). We defined the increase in image contrast as the increase in s.d. of the energy-normalized histogram (Online Methods). Penetration depths measured for DSLM-SI agreed with the theoretically expected values (**Supplementary Fig. 6**), indicating that DSLM-SI contrast improvement does not occur at the expense of penetration depth into the specimen. A comparison of the depths characterizing exponential signal decay for structured-illumination frequencies

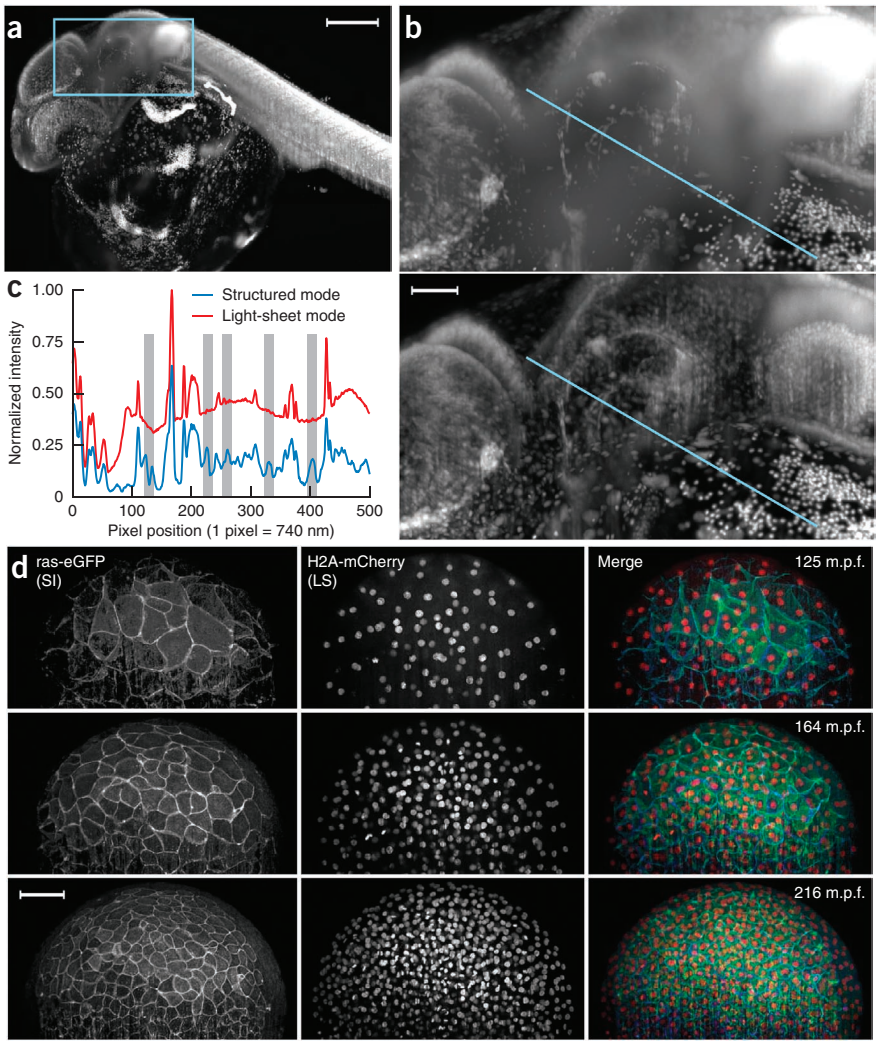

Figure 2 | Enhancing image contrast with DSLM-SI. (**a**) Maximum-intensity projection of a DSLM image stack of a 3.5-day old Medaka fish embryo with Sytox Green nuclear staining, recorded with standard light-sheet illumination (10× magnification). Stack dimensions are 435 images, recorded at a *z*-dimension spacing of 3 µm, covering a total volume of 1,516 µm × 1,516 µm × 1,305 µm. (**b**) Magnification of the boxed region in **a**, recorded in standard light-sheet mode (top) and in structured-illumination mode (SI frequency $s = 32$; SI-32; bottom). (**c**) Intensity plot along the lines indicated in **b**. In both plots, the raw intensity values were normalized by the same factor (global maximum of both images). Shading highlights structures in the structured-illumination image that are not visible in the light-sheet mode image. (**d**) Maximum-intensity projections of a DSLM time-lapse recording of a membrane- and nuclei-labeled zebrafish embryo injected with *ras-eGFP* mRNA and *H2A-mCherry* mRNA at the one-cell stage. Membranes were imaged using structured illumination (SI frequency $s = 25$; SI-25), and nuclei were imaged using standard light sheet illumination (LS). (m.p.f., minutes post fertilization.) Images were deconvolved with ten iterations of the Lucy-Richardson algorithm[20]. Scale bars, 200 µm (**a**), 50 µm (**b**) and 100 µm (**d**). Fluorescence was detected with a Carl Zeiss C-Apochromat 10×/0.45 W objective**.** Recording speeds were six DSLM images per second and two structured illumination–reconstructed images per second.

between 2.7 and 50 demonstrated a variability of only 10.6% in penetration depth for the entire range of practical frequencies (**Supplementary Fig. 6**).

We next applied DSLM-SI to the three-dimensional imaging of large, nuclei-stained Medaka fish embryos at different levels of magnification (**Fig. 2a**,**b** and **Supplementary Fig. 8**). The observed increase in image contrast and the removal of scattered light translated directly into an enrichment in information quality, revealing specimen features that were less bright than the scattered light component in the standard light-sheet recording (**Fig. 2c**). The benefits applied to the entire range of practicable magnifications (for example, 10×, 20× and 63×; **Supplementary Fig. 8**) but required different structured-illumination frequencies for optimal image contrast.

The high imaging speeds and very low photobleaching rates achieved in DSLM-SI were crucial for *in vivo* imaging of development, particularly when using markers for morphologically complex structures that need to be visualized at a good contrast, such as membrane markers, or when recording for very long periods of time.

High-speed, long-term imaging of zebrafish development

We recorded nuclei and membrane markers in an early zebrafish embryo, by switching between standard light-sheet illumination for the nuclei channel and DSLM-SI for the membrane channel (**Fig. 2d**). The 480 images required to capture both markers in three dimensions could be recorded within 90 s, a temporal sampling previously shown to enable comprehensive cell tracking[6]. The complete dataset of the 6.5-h acquisition period (2–8.5 h post fertilization (h.p.f.)) comprised 125,280 images (**Supplementary Video 2**). To demonstrate complete coverage of the embryo, we provide a panel of single planes (**Supplementary Fig. 9**).

We also performed long-term DSLM-SI imaging of a membrane-labeled zebrafish from 9 h.p.f. to 67 h.p.f. We recorded three views of the specimen at 3-min intervals, collecting 960,480 images over 58 h. One of these views shows eye development and midbrain neurogenesis (**Supplementary Video 3**). Single DSLM-SI planes (**Supplementary Figs. 10–12**) demonstrated full penetration of the head of the one-day-old embryo, including forebrain, midbrain and both eyes. Using DSLM-SI, we obtained an average increase of 82% in image contrast in the zebrafish embryo (**Supplementary Fig. 12b–d**). In addition to providing increased contrast, DSLM-SI also eliminated out-of-focus structures from the images, thus increasing the qualitative and quantitative information content of the images (**Supplementary Fig. 12a**).

High-speed imaging of early *Drosophila* embryogenesis

Although standard light-sheet microscopy allows recording of early zebrafish development in its entirety[6], it does not allow collection of similar-quality data for less transparent model organisms. For example, imaging a transgenic *Drosophila* strain with the same nuclear marker resulted in images with low contrast and a

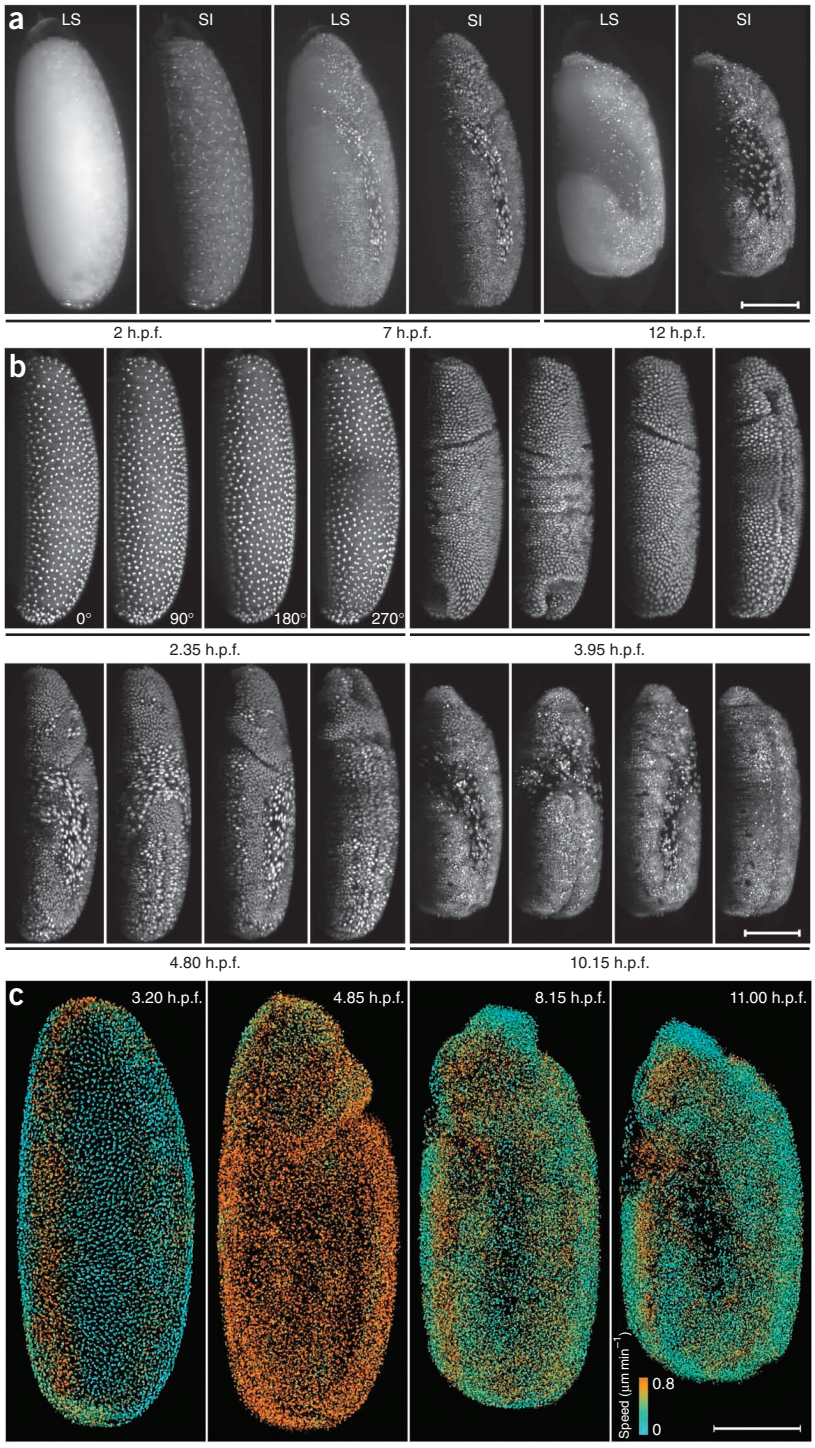

Figure 3 | Multiple-view imaging of *Drosophila* embryogenesis with DSLM-SI. (**a**) Maximum-intensity projections of DSLM image stacks of a nuclei-labeled *Drosophila* embryo, using standard light-sheet illumination (LS, left) and structured illumination (SI frequency $s = 20$; SI-20; right) at the indicated times. The image pairs show the same volume at the same time point. (**b**) Maximum-intensity projections of a DSLM-SI multiple-view time-lapse recording of a nuclei-labeled *Drosophila* embryo at the indicated times. Images were deconvolved with the Lucy-Richardson algorithm (five iterations). (**c**) Lateral snapshots of the fly digital embryo. Nuclei were automatically detected in the four views of the developing *Drosophila* embryo. The resulting point clouds were fused. Color bar indicates directed regional nuclei movement speeds over 10-min periods. Scale bars, 100 μm. Fluorescence was detected with a Carl Zeiss Plan-Apochromat 20×/1.0 W objective. Recording speeds were six DSLM images per second and two structured illumination reconstructed images per second.

considerable contribution of scattered fluorescence light from out-of-focus structures (**Fig. 3a** and **Supplementary Fig. 13**). The resulting datasets were, therefore, less well suited for subsequent automated image processing. Using DSLM-SI we collected high-contrast images and removed out-of-focus structures, which can contribute false positives to subsequent segmentation of the datasets (**Fig. 3b**,**c** and **Supplementary Fig. 13**). We observed an average increase in image contrast of 261% by using DSLM-SI to image the early *Drosophila* embryo (**Supplementary Fig. 13**). We also assessed the penetration depth in the DSLM-SI recording at embryonic stage 6 and determined a 50% signal decay at a depth of 38.0 ± 3.8 μm (**Supplementary Fig. 14**). The value we obtained for DSLM-SI was slightly higher than values previously reported for conventional two-photon fluorescence microscopy at stages 5 and 8 for the same type of specimen[17], indicating that coverage in DSLM-SI is outstanding.

For maximum coverage, we recorded multiple-view time-lapse datasets of *Drosophila* embryos with labeled nuclei from 2 h.p.f. to 11.5 h.p.f. with 3-min intervals for all four views. The maximum-intensity projections (**Fig. 3b**) were based on 720 DSLM-SI images for each time point; the complete dataset comprised 137,520 images (**Supplementary Video 4**).

Contrast optimization by DSLM-SI frequency chirp

The *Drosophila* embryo is well suited to illustrate a key advantage provided by the flexibility arising from the DSLM-based implementation of structured illumination. Owing to the electronic modulation underlying the structured-illumination pattern generation, we realized a high-speed structured-illumination frequency chirp mode, in which we recorded each plane in the specimen using multiple patterns with different structured-illumination frequencies (**Fig. 4a**,**b**). This use of the term 'chirp' refers to the rapid change of modulation frequency of the spatial illumination pattern: to obtain the maximum image contrast, the structured-illumination frequency must be adjusted as a function of imaging depth in the specimen and as a function of time during *Drosophila* embryonic development. A contrast enhancement of at least 100% resulted for all structured-illumination frequencies $s \geq 15$ per field of view (except for surface structures, which required $s \geq 30$ per field of view; **Fig. 4c**). We achieved the optimum by minimizing

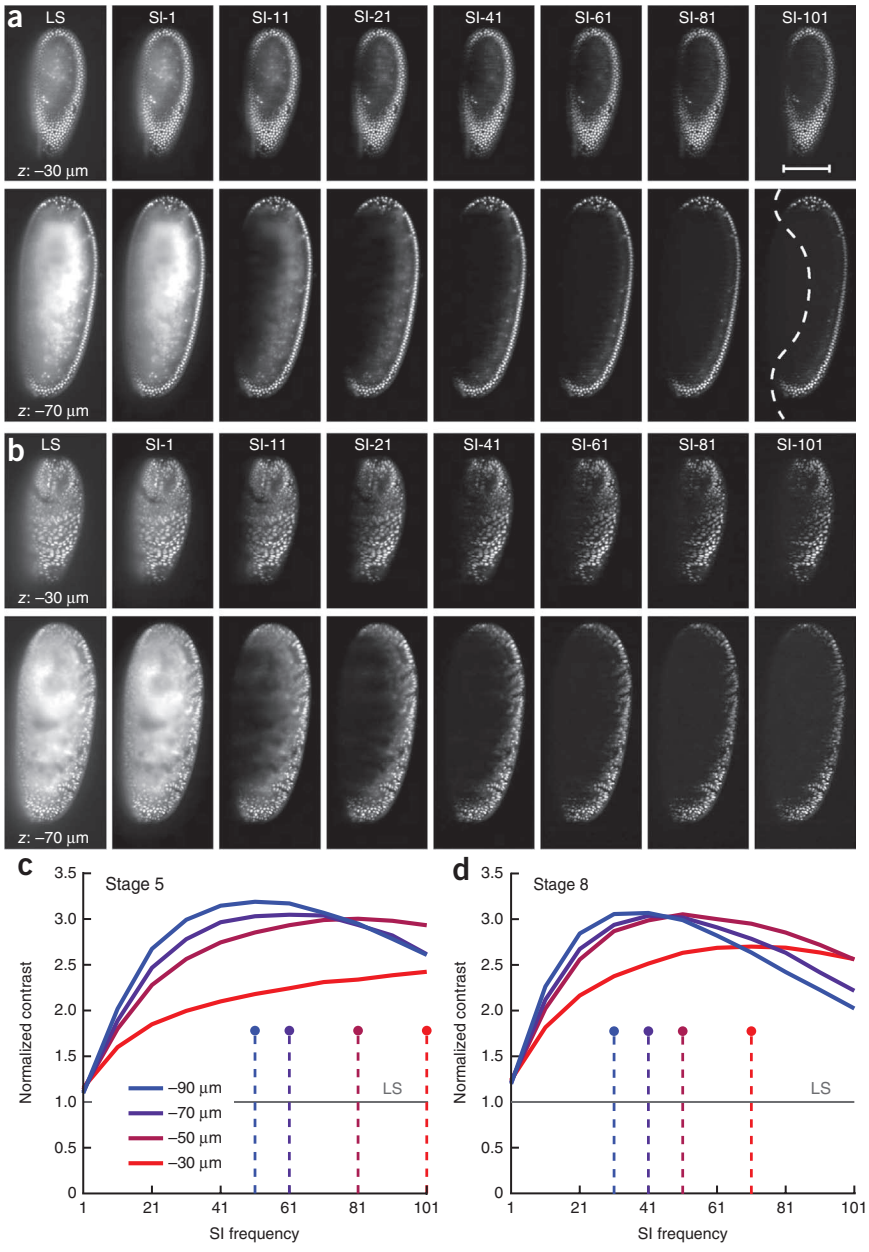

Figure 4 | Spatiotemporal image contrast optimization by DSLM-SI frequency chirping. (**a**,**b**) DSLM images of a nuclei-labeled stage 5 *Drosophila* embryo (before internal structures have developed; **a**) and at stage 8 (**b**) at two different depths (*z*) inside the specimen, using standard light-sheet illumination (LS) and structured-illumination patterns with different frequencies (SI-1 to SI-101). The dashed line separates the region containing the background and out-of-focus signal that has been removed by DSLM-SI (left) from the in-focus structures where the contrast has been enhanced (right). Scale bar, 100 µm. Fluorescence was detected with a Carl Zeiss Plan-Apochromat 20×/1.0 W objective. Recording speeds were five DSLM images per second and 1.7 structured illumination–reconstructed images per second. (**c**,**d**) Quantification of image contrast as a function of structured-illumination frequency at the indicated imaging depths inside the specimen, for the time points shown in **a** and **b**, respectively. The horizontal line indicates the image contrast obtained with standard light-sheet illumination (LS). Colored spheres indicate structured-illumination frequencies for which the maximum image contrast was obtained.

the scattered light contribution in the reconstructed image without compromising the signal-to-noise ratio. The higher the structured-illumination frequency, the lower the scattered light contribution, but the fraction of removed nonscattered signal photons also increased with the structured-illumination frequency. The optical transfer function of the illumination subsystem modulates the sine wave pattern and, therefore, increases the intensity baseline in the structured-illumination profile. The optical properties of the specimen additionally modulate the pattern. Close to the surface of the specimen, high structured-illumination frequencies provide the best image contrast (~100 per field of view at a detection depth of 30 µm; **Fig. 4c**). Deep inside the specimen, however, lower frequencies were required (frequencies of ~80, 60 and 50 per field of view at detection depths of 50, 70 and 90 µm, respectively; **Fig. 4c**), particularly as light scattering increased during later stages of development (frequencies of ~70, 50, 40 and 30 per field of view at stage 8 compared to ~100, 80, 60 and 50 per field of view at stage 5, for detection depths of 30, 50, 70 and 90 µm, respectively; **Fig. 4d**). Because different structured-illumination frequencies are required to obtain the optimal contrast in different parts of the specimen and at different time points during development, the capability of DSLM-SI to quickly adjust the pattern frequency allows real-time spatiotemporal optimization of image contrast for time-lapse recordings of live embryos.

The *Drosophila* digital embryo

Our DSLM-SI images of the early nuclei-labeled *Drosophila* embryo provide precise information on cell positions over time at a contrast sufficient for automated image processing (**Supplementary Fig. 15**). To illustrate the potential of the recordings, we developed segmentation algorithms based on the Laplacian of a Gaussian blob detection method[18] and determined center-of-mass positions and approximate diameters of the nuclei from the DSLM-SI image stacks to transform the enhanced GFP (eGFP) intensity distributions into a digital reconstruction of each view of the embryo (**Supplementary Data 1**). We then used the iterative closest-point algorithm[19] to obtain the affine transformation that properly aligned the segmented data in the four views (**Supplementary Fig. 16** and **Supplementary Video 5**) and fused the information into a single digital dataset, the fly digital embryo, with ~1.5 million nucleus data entries (**Fig. 3c**, **Supplementary Video 6** and **Supplementary Data 2**). An analysis of the segmentation efficiency and volumetric coverage (determined from axial cross-sections of the digital embryo at different time points and at different lateral offsets) showed that the fly digital embryo comprised ~95% of the embryo's nuclei for 2–4.5 h.p.f.,

73% for 4.5–7 h.p.f. and 54% for 7–11.5 h.p.f. Volumetric coverage decreased once the formation of inner structures commenced. In fact, 90% of the missing nuclei corresponded to the innermost structures of the embryo that were difficult to resolve owing to physical limitations of the penetration depth at visible wavelengths in the light microscope.

The fly digital embryo database and all videos are available in the Digital Embryo online repository at http://www.digital-embryo.org/.

DISCUSSION

The quantitative and qualitative improvements in image quality we achieved in DSLM-SI cannot be reproduced by current computational post-processing solutions. Both the morphology and the optical properties of live specimens are highly complex, constantly changing and effectively unknown. Therefore, it is very difficult to define a model of light scattering and absorption of the entire recorded organism that would be sufficiently accurate to obtain improvements in image quality similar to those in DSLM-SI. Even if one implemented an approximate biophysical model, it would still hold the risk of biasing the data compared to the direct physics-based solution. Post-processing solutions are also computationally expensive. We performed the DSLM-SI reconstructions such as the 8-terabyte DSLM-SI dataset shown in **Supplementary Video 3** in real time, but modeling and applying a spatially variant deconvolution kernel to the approximately one million images of this dataset would be much more costly.

Compared to SPIM-SI, DSLM-SI has three major advantages. First, the AOTF allows fast modulation of the illuminating laser beam and thus rapid image acquisition using phase-shifted illumination patterns. Second, exceptionally high quality and stability of the illumination pattern for long-term imaging can be achieved by avoiding optical grids that may drift. Third, the flexibility in creating illumination patterns with different spatial frequencies allows one to optimally address spatial and temporal changes in light scattering during development of live specimens.

Our fly digital embryo shows the cellular dynamics of development in an almost complete early *Drosophila* embryo. But in the context of comprehensive cell-lineage reconstructions, a higher temporal resolution of about 30 s by using faster cameras would be advantageous. Our approach to imaging and reconstructing embryogenesis in nontransparent species has several applications: describing morphogenesis of embryos from species that have been poorly analyzed to date, characterizing the phenotypes of mutants, creating a morphogenetic scaffold for mapping and comparing gene expression data, obtaining detailed quantitative information on cell migratory tracks and cell division patterns for biophysical modeling of cell behavior and assembling a comprehensive data basis for establishing and testing computer models of embryogenesis. The intrinsic elimination of scattered signal fluorescence provided by DSLM-SI is invaluable for the robust automated image processing and subsequent data analyses essential for such applications.

METHODS

Methods and any associated references are available in the online version of the paper at http://www.nature.com/naturemethods/.

Note: Supplementary information is available on the Nature Methods website.

ACKNOWLEDGMENTS

We thank members of the mechanical workshop of the European Molecular Biology Laboratory for custom hardware; A. Riedinger and G. Ritter for custom electronics; F. Härle and A. Riedinger for custom microscope software; J. Topczewski (Northwestern University) for the *ras-eGFP* zebrafish strain; M. Ludwig and K. White (University of Chicago) for the *histone-eGFP Drosophila* strain; and A. Diaspro, F. Cella and P. Theer for helpful discussions. Financial support was provided to A.D.S. by Hartmut Hoffmann-Berling International Graduate School of Molecular and Cellular Biology.

AUTHOR CONTRIBUTIONS

P.J.K. and E.H.K.S. conceived the research. P.J.K. implemented DSLM-SI, conducted the *Drosophila* experiments, performed the reconstructions, analyzed the DSLM-SI data and wrote the paper. P.J.K., A.D.S. and J.W. conducted the zebrafish experiments. P.J.K., A.S., K.K. and Z.B. constructed the fly digital embryo. All authors commented on the manuscript.

COMPETING FINANCIAL INTERESTS

The authors declare competing financial interests: details accompany the full-text HTML version of the paper at http://www.nature.com/naturemethods/.

Published online at http://www.nature.com/naturemethods/.
Reprints and permissions information is available online at http://npg.nature.com/reprintsandpermissions/.

1. Bao, Z. *et al.* Automated cell lineage tracing in *Caenorhabditis elegans*. *Proc. Natl. Acad. Sci. USA* **103**, 2707–2712 (2006).
2. Megason, S.G. & Fraser, S.E. Imaging in systems biology. *Cell* **130**, 784–795 (2007).
3. Fowlkes, C.C. *et al.* A quantitative spatiotemporal atlas of gene expression in the *Drosophila* blastoderm. *Cell* **133**, 364–374 (2008).
4. McMahon, A., Supatto, W., Fraser, S.E. & Stathopoulos, A. Dynamic analyses of *Drosophila* gastrulation provide insights into collective cell migration. *Science* **322**, 1546–1550 (2008).
5. Murray, J.I. *et al.* Automated analysis of embryonic gene expression with cellular resolution in *C. elegans*. *Nat. Methods* **5**, 703–709 (2008).
6. Keller, P.J., Schmidt, A.D., Wittbrodt, J. & Stelzer, E.H.K. Reconstruction of zebrafish early embryonic development by scanned light sheet microscopy. *Science* **322**, 1065–1069 (2008).
7. Keller, P.J. & Stelzer, E.H. Quantitative in vivo imaging of entire embryos with digital scanned laser light sheet fluorescence microscopy. *Curr. Opin. Neurobiol.* **18**, 624–632 (2008).
8. Long, F., Peng, H., Liu, X., Kim, S.K. & Myers, E. A 3D digital atlas of *C. elegans* and its application to single-cell analyses. *Nat. Methods* **6**, 667–672 (2009).
9. Liu, X. *et al.* Analysis of cell fate from single-cell gene expression profiles in *C. elegans*. *Cell* **139**, 623–633 (2009).
10. Neil, M.A., Juskaitis, R. & Wilson, T. Method of obtaining optical sectioning by using structured light in a conventional microscope. *Opt. Lett.* **22**, 1905–1907 (1997).
11. Huisken, J., Swoger, J., Del Bene, F., Wittbrodt, J. & Stelzer, E.H.K. Optical sectioning deep inside live embryos by selective plane illumination microscopy. *Science* **305**, 1007–1009 (2004).
12. Breuninger, T., Greger, K. & Stelzer, E.H. Lateral modulation boosts image quality in single plane illumination fluorescence microscopy. *Opt. Lett.* **32**, 1938–1940 (2007).
13. Frohn, J.T., Knapp, H.F. & Stemmer, A. True optical resolution beyond the Rayleigh limit achieved by standing wave illumination. *Proc. Natl. Acad. Sci. USA* **97**, 7232–7236 (2000).
14. Gustafsson, M.G. Surpassing the lateral resolution limit by a factor of two using structured illumination microscopy. *J. Microsc.* **198**, 82–87 (2000).
15. Gustafsson, M.G. Nonlinear structured-illumination microscopy: wide-field fluorescence imaging with theoretically unlimited resolution. *Proc. Natl. Acad. Sci. USA* **102**, 13081–13086 (2005).
16. Kner, P., Chhun, B.B., Griffis, E.R., Winoto, L. & Gustafsson, M.G. Super-resolution video microscopy of live cells by structured illumination. *Nat. Methods* **6**, 339–342 (2009).
17. Supatto, W., McMahon, A., Fraser, S.E. & Stathopoulos, A. Quantitative imaging of collective cell migration during *Drosophila* gastrulation: multiphoton microscopy and computational analysis. *Nat. Protocols* **4**, 1397–1412 (2009).
18. Marr, D. & Hildreth, E. Theory of edge detection. *Proc. R. Soc. Lond. B* **207**, 187–217 (1980).
19. Besl, P.J. & McKay, N.D. A method for registration of 3-D shapes. *IEEE Trans. Pattern Anal. Mach. Intell.* **14**, 239–256 (1992).
20. Richardson, W.H. Bayesian-based iterative method of image restoration. *J. Opt. Soc. Am.* **62**, 55–59 (1972).

ONLINE METHODS

DSLM-SI implementation. A homogeneous DSLM illumination profile equivalent to a light sheet in SPIM was obtained by applying a constant scan speed and a constant laser power during sample illumination[6]. The introduction of either a periodic variation of the scan speed or a laser intensity modulation function resulted in a patterned illumination profile. Thereby, different lines along the sample were illuminated with different intensities (**Fig. 1b**). Our implementation of the DSLM-SI is based on a laser intensity modulation during the scan process. The modulation of the voltage driving the AOTF radio frequency input signal creates a sinusoidal intensity modulation as a function of time. The sigmoidal AOTF voltage-response function is measured and used to obtain the best estimate for a sinusoidal intensity output. In the structured-illumination mode, the DSLM records three 120° phase-shifted images per sample plane. This set of three images is then combined into a single image by a straight-forward mathematical procedure (equation 1). As the laser modulation follows a sinusoidal function and three images are required to reconstruct the information in one object plane, the total energy exposure of the specimen is increased by 50% compared to the standard light-sheet illumination mode. In practice, the increase of the intensity baseline resulting from the optical transfer function necessitates an additional structured illumination frequency–dependent increase in illumination energy to obtain images of the same brightness. Using a pco.2000 camera (PCO AG) with a maximum recording rate of 15 frames per second (using two analog-to-digital converters) and a chip size of 2,048 pixels × 2,048 pixels, the DSLM produces a maximum of five reconstructed planes per second in its structured-illumination mode, which corresponds to an imaging speed of 20 million voxels per second.

The DSLM-SI patterns are created by using the following hardware components: an AA.AOTF.nC-400-650nm-PV-TN AOTF (AA Opto-Electronic), a pair of VM-500+ laser scanners operated via an HC/3 scan controller (GSI Lumonics), an S4LFT0061 F-theta lens with 60-mm focal length (Sill Optics), a tube lens with 164.5-mm focal length (Carl Zeiss), an NI-6733 data acquisition board (National Instruments) and a Plan-Apochromat 5×/0.16 W illumination lens (Carl Zeiss). We equipped the DSLM with the following detection lenses: C-Apochromat 10×/0.45 W, Plan-Apochromat 20×/1.0 W and Plan-Apochromat 63×/1.0 W (Carl Zeiss).

Our DSLM-SI implementation is inexpensive and straightforward to recapitulate. We provide an annotated photograph of the central part of the instrument in **Supplementary Figure 1**.

DSLM-SI parameters and acquisition settings. To obtain DSLM-SI patterns with a spatial frequency f_{stripes}, the DSLM scan mirror was operated at a constant tilt speed v_{mirror}, while the laser intensity is modulated according to a sine function with frequency f_{AOTF} at the AOTF radio input. Using the structured-illumination frequency parameter s provided throughout this paper, the spatial pattern frequency resulted as $f_{\text{stripes}} = s/h$, where h is the height of the light sheet. For a 10× field of view (FOV), such as that in **Figure 1b**, the height of the light sheet was set to 1,650 µm. Our definition of h scaled linearly with the magnification in the detection arm, that is, the corresponding light-sheet height for a 20× FOV was 825 µm and so on. Practical values for f_{stripes} at 10× magnification therefore ranged between 0.6 mm^{-1} ($s = 1$) and 60 mm^{-1} ($s = 100$), corresponding to center-to-center distances between 1,650 µm ($s = 1$) and 16.5 µm ($s = 100$).

The exposure time was set to $t = 50$ ms in all experiments, except for those in **Figure 4**, in which $t = 100$ ms. Thus, the temporal modulation frequencies $f_{\text{AOTF}} = s/t$ ranged between 20 Hz ($s = 1$) and 2 kHz ($s = 100$) for all experiments, except for those in **Figure 4** in which the range of f_{AOTF} was 10 Hz ($s = 1$) to 1 kHz ($s = 100$). The AOTF amplitude modulation was synchronized with the movement of the scan mirror. In the DSLM-SI mode, the FOV was scanned once per exposure time interval. Hence, the scan speed for a 10× FOV $v_{\text{beam}} = 33$ mm s^{-1} at $t = 50$ ms (vertical displacement speed of laser beam in the specimen), corresponding to a tilt speed $v_{\text{mirror}} = 78\,° \text{ s}^{-1}$ of the scan mirror (156 ° s^{-1} optical tilt speed), and $v_{\text{beam}} = 16.5$ mm s^{-1} at $t = 100$ ms, corresponding to $v_{\text{mirror}} = 39\,° \text{ s}^{-1}$ (78 ° s^{-1} optical tilt speed). When using an F-theta lens, the formula relating mirror tilt speed v_{mirror} and beam scan speed v_{beam} was calculated as follows:

$$v_{\text{mirror}} = \frac{90}{\pi}\frac{M}{f}v_{\text{beam}} \qquad (2)$$

in which M is the magnification of the illumination objective and f is the focal length of the F-theta lens. For our set-up, $M = 5$ and $f = 60.52$ mm.

The light-sheet full-width half maximum (FWHM) thickness was set to 4 µm (standard thickness in our setup in the absence of a beam expander) to obtain the maximum average axial resolution across the FOV with a single alignment for both *Drosophila* and zebrafish recordings. According to this criterion, a FWHM thickness of 3.26 µm is optimal for imaging *Drosophila* embryos (FOV, 250 µm), whereas a FWHM thickness of 5.06 µm is optimal for imaging early zebrafish embryos (FOV, 600 µm). Note that the Rayleigh criterion, an alternative criterion for defining optimal light-sheet properties, would suggest FWHM values of 4.50 µm and 6.97 µm, respectively. At a 10× magnification of the detection objective, the vertically scanned DSLM laser beam illuminates a stripe corresponding to $n \approx 6$ lines on the CCD camera chip at any given time point (assuming a light-sheet FWHM thickness of 4 µm and a pixel pitch of 7.4 µm on the CCD camera). In a perfect alignment, the optimal light sheet thickness is proportional to the inverse of the square root of the magnification in the detection subsystem. Hence, n is proportional to the square root of the magnification in the detection subsystem, that is, $n \geq 6$ for magnifications ≥ 10×. At $t = 50$ ms exposure time, the DSLM line dwell time is therefore ≥ 150 µs for a detection magnification ≥ 10×, when using a CCD camera chip with 2,048 horizontal lines. Using a pco.2000 camera, a 50 ms exposure time and a single analog-to-digital converter for increased image quality, approximately six frames were recorded per second, that is, two complete structured illumination–reconstructed images were obtained per second.

Comparative analysis of image contrast. To compare image contrast in DSLM-SI and conventional light-sheet recordings, we calculated the increase in s.d. of the energy-normalized histograms of the DSLM and DSLM-SI image pairs. Let c_i be the pixel count for intensity level i in an image (with i ranging between gray levels 0 and 10,000 when using a pco.2000 camera).

The complete set of pairs (i, c_i) then defines the intensity histogram of this image. Using the image intensity integral

$$I = \sum_i i \times c_i, \tag{3}$$

the total pixel count

$$C = \sum_i c_i \tag{4}$$

and the average intensity of the image

$$\bar{I} = I/C, \tag{5}$$

the s.d. of the energy-normalized image histogram is defined as:

$$\sigma = \sqrt{\frac{\sum_i \left(c_i \times \left(\frac{i - \bar{I}}{I} \right)^2 \right)}{C - 1}} \tag{6}$$

Owing to the energy normalization, the σ values of the DSLM and DSLM-SI image pairs are directly comparable and their ratio reflects an objective measure of the change in image contrast (**Fig. 4c**,**d** and **Supplementary Figs. 6**, **7**, **12** and **13**).

Preparation, characterization and imaging of tissue phantoms. Tissue phantoms were created by adding fluorescein-containing polystyrene latex beads (Polysciences, Fluoresbrite Plain YG 0.75 µm, stock concentration 1.206×10^{11} ml^{-1}) and nonfluorescent polystyrene latex beads (Polysciences, Polybead Polystyrene 0.75 µm, stock concentration 1.117×10^{11} ml^{-1}) to 1.5% low-melting-temperature agarose (**Supplementary Fig. 5**). The bead diameter of 750 nm was chosen to obtain an average cosine of the phase function $g = 0.926$, which is close to values measured for actual neural tissues at a wavelength of 500 nm, such as the pons ($g = 0.91$) or gray matter ($g = 0.88$)[21]. We created tissue phantom with seven different scattering coefficients μ_s = 1, 1.5, 2, 3, 5, 10 and 15 mm^{-1}. This range covers scattering coefficients previously measured for neural tissues (μ_s = 10.99 mm^{-1} for gray matter, μ_s = 13.37 mm^{-1} for pons; illumination wavelength: 500 nm)[21] and also includes phantoms with optical penetration depths similar to those observed in zebrafish and *Drosophila* embryonic tissues at 488 nm. Different scattering coefficients were obtained by adjusting the concentration of scattering beads. An overview of the optical properties of the phantoms is provided in **Supplementary Table 1**. We recorded and analyzed DSLM-SI images of all seven phantoms as a function of detection depth in the specimen (0–1,000 µm, in steps of 10 µm) and frequency of the structured-illumination pattern (structured-illumination frequencies 2.7–50; SI-2.7 to SI-50). Note that the center-to-center distances between SI intensity maxima were 306 µm at the lowest frequency, SI-2.7, and 16.5 µm at the highest frequency, SI-50. Analysis of the DSLM-SI phantom images provided a characterization of the contrast enhancement, penetration depth and subtracted light fraction as a function of DSLM-SI pattern frequency, imaging depth and phantom scattering coefficient (**Supplementary Figs. 6** and **7**).

Medaka and zebrafish preparation and imaging. Medaka embryos were fixed in 4% paraformaldehyde and stained for nuclei with Sytox Green (**Fig. 2a–c** and **Supplementary Fig. 8**). Zebrafish wild-type embryos were dechorionated at the one-cell stage and injected with 20 µM *H2B-mCherry* mRNA and 20 µM *ras-eGFP* mRNA (**Fig. 2d**, **Supplementary Fig. 9** and **Supplementary Video 2**). Embryos of the *ras-eGFP* transgenic line were dechorionated at the one-cell stage (**Supplementary Figs. 10** and **11**, and **Supplementary Video 3**). Stained Medaka embryos and injected or transgenic zebrafish embryos were embedded in 1% low-melting-temperature agarose as previously described[6]. The DSLM imaging chamber was filled with 30% Danieau's buffer (for live zebrafish imaging) or 1× PBS (for fixed Medaka embryos).

DSLM or DSLM-SI imaging was performed using the 488 nm and 568 nm lines of an Argon-Krypton gas laser (Melles Griot) for illumination and RazorEdge 488 RU and 568 RU long-pass filters (Semrock) in the detection system. DSLM-SI frequencies were applied as stated in the figure or movie legends. For volumetric imaging, images were acquired with a 4-µm-thick light sheet (FWHM) in steps of 1.8 µm (**Supplementary Fig. 8c**,**d**), 3 µm (**Fig. 2a**,**b** and **Supplementary Fig. 8a**,**b**) or 3.7 µm (**Fig. 2d**, **Supplementary Figs. 9–12** and **Supplementary Videos 2** and **3**). The exposure time was set to 50 ms per image for all experiments. In the experiment underlying **Supplementary Video 2**, manual laser power adjustments were applied to prevent image saturation resulting from H2A-mCherry and ras-eGFP production (stepwise reduction of 488 nm laser power from 90% to 7%, step-wise reduction of 568 nm laser power from 90% to 5%). In the experiment underlying **Supplementary Video 3**, manual laser power adjustments were applied to maintain constant image brightness (stepwise increase of 488 nm laser power from 20% to 40% over a period of 3 d). The specimen position along the vertical axis was manually corrected to compensate for the drift of the agarose cylinder during the first few hours of imaging. Typically, a total drift distance of up to 50 µm occurred over a period of 3 h before the vertically mounted agarose matrix was fully equilibrated.

***Drosophila* preparation and imaging.** H2B-eGFP transgenic *Drosophila* embryos were dechorionated with 5% sodium hypochlorite solution. Glass capillaries (Brand) were filled with liquid 1% low-melting-temperature agarose using Teflon piston rods (Brand). Before polymerization of the agarose network, dechorionated embryos were carefully transferred to the capillary and oriented along the axis using forceps (Dumont). After polymerization, excess agarose below the embryo was removed with a razor blade. For DSLM and DSLM-SI imaging, the capillary was inserted in the sample holder and placed in the sample chamber loaded with 1× PBS buffer. The lower part of the agarose cylinder was then pushed out with the piston rod to expose the embryo to the laser illumination pattern. Specimen preparation was performed at 20 °C, and the temperature of the sample chamber was set to 24 °C for live imaging (from 2 h.p.f. onward).

To achieve good coverage at high temporal sampling rates, four views of the embryo were recorded (0°, 90°, 180° and 270°). DSLM-SI frequencies were applied as stated in the figure and movie legends. Images were acquired with a 4-µm-thick light sheet (FWHM) in 3.7-µm steps. The exposure time was set to 50 ms

doi:10.1038/nmeth.1476

(**Fig. 3a**,**b**, **Supplementary Figs. 13** and **14** and **Supplementary Video 4**) or 100 ms (**Fig. 4**) per image. In the experiment underlying **Supplementary Video 4**, manual laser power adjustments were applied to prevent image saturation resulting from histone-eGFP production (stepwise reduction of 488 nm laser power from 50% to 20%). Manual corrections of the specimen position along the vertical axis were applied as described above for zebrafish imaging.

***Drosophila* segmentation and fusion.** An overview of the processing workflow for data visualization and construction of the digital embryo is provided in **Supplementary Figure 15**.

Reconstructed images were filtered with a three-dimensional (3D) difference of Gaussians filter[18] with a frequency matched to the expected average nuclear size. Nuclear size is set manually at the first time point and updated from calculated nuclear boundaries at each successive time point. The filter serves as a blob detector, smoothing noise and local fluorescence variation and emphasizing blobs of the expected size. In classical blob detection, a threshold is applied and the brightest points in three dimensions are assumed to be nuclear centers. This, however, overlooks dimmer nuclei that are masked by brighter neighbors nearby. We developed a modified extraction method, enabling these nuclei to be detected and also segmenting an explicit nuclear boundary.

Pixels that are local maxima in a 2D image slice are the seed points of individual slices through a nucleus. The subset of these, which are also maxima in three dimensions, are the centers of the nuclei. Each 2D slice is segmented by sending 16 uniformly distributed rays out from the maximum. Rays stop when they encounter a pixel with a value less than half the value at the maximum. The endpoints of these rays define a polygonal boundary for the slice. Starting at each 3D maximum slice, which is a nuclear center, nearby slices were grouped with that nucleus, if they match a model of expected slice size, maximum intensity and position. Once all detected nuclei have been extracted, overlooked nuclei are inserted wherever a cluster of unclaimed slices occurs, and nuclei with largely overlapping slice sets are merged (**Supplementary Data 1**). The final result is a set of nuclei, each of which is a collection of 2D polygonal boundaries. For visualization purposes a bounding sphere is output for each nucleus.

The relative alignment of the four independently segmented views of the *Drosophila* embryo was achieved by global optimization of the parameters of an affine matrix transformation (**Supplementary Fig. 16**). Optimization was performed with the iterative closest-point algorithm[19]. After aligning the segmented data in the four views, the information was fused into a single digital dataset, the fly digital embryo (**Supplementary Data 2**). Redundant data entries in the overlap regions were eliminated by using the criterion of conservation of the global minimal distance of nucleus pairs before (in the individual views) and after fusion (in the combined dataset).

Rendering of the digital embryo and determination of cell migration vectors were performed with our custom processing pipeline, as described before[6]. For color-coding of tissue movements (**Supplementary Video 6**), local population-statistical averages of the cell migration vectors were calculated and mapped to a linear look-up table.

Coverage of the fly digital embryo. We performed manual controls for false positives and false negatives in the segmentation database at time points 40 and 90 (corresponding to 4 h.p.f. and 6.5 h.p.f., respectively), and determined a maximum segmentation error rate of 5%. Between time points 0 and 50 (corresponding to 2 h.p.f. and 4.5 h.p.f., respectively), that is, between the arrival of the first nuclei at the embryonic surface and the internalization of mesoderm at the ventral furrow, the volumetric coverage of nuclei-containing regions in the specimen was approximately 100%. Beyond time point 50, the volumetric coverage in the light-microscopic recording was determined by fitting ellipsoids to the outer and inner shell of the segmented point clouds. The fraction of missing nuclei was defined as the ratio of the inner ellipsoidal volume and the outer ellipsoidal volume. For time points 100, 150 and 190 (corresponding to 7 h.p.f., 9.5 h.p.f. and 11.5 h.p.f., respectively), we obtained a volumetric coverage of 51%, 55% and 56%, respectively. The coverage between time points 50 and 100, that is, between the onset of internalization and application of the first volumetric reference ratio, was linearly interpolated. Note that these numbers represent an underestimate of the true physiological coverage, since they are based on the assumption of a uniform nuclear density throughout the specimen. The slight increase in coverage between time points 100 and 190 can be explained by the slowly increasing transparency of the embryo at later stages of embryogenesis.

Combining the minimum segmentation efficiency (95%) with the temporally averaged volumetric coverage (74%) provides an estimated 70% overall nuclear coverage in the fly digital embryo.

21. Yaroslavsky, A.N. *et al.* Optical properties of selected native and coagulated human brain tissues in vitro in the visible and near infrared spectral range. *Phys. Med. Biol.* **47**, 2059–2073 (2002).